HRTEM Analysis of the Influence of Non-stick Coal's Oxidation Degree on Aromatic Fringe Morphology

Jiajun Li, Guochao Yan,* Shaoqi Kong,* Zhen Li, Gang Li, Xuyang Bai, and Jiawei Zhang
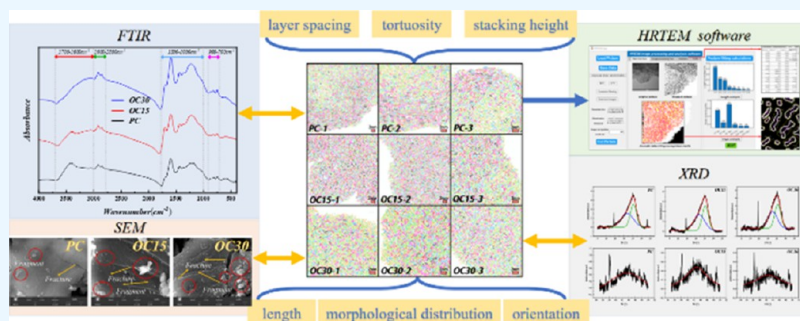
Read Online

ACCESS | Metrics & More | Article Recommendations

ABSTRACT: The purpose of this research was to explore the parameters of the aromatics lattice fringes by using high resolution transmission electron microscopy (HRTEM) patterns, combined with ArcGIS and MATLAB methods, to quantitatively evaluate and analyze the coal samples oxidized by different concentrations of H_2O_2, and to explore the changes in the morphology and spatial distribution of the aromatic system under oxidation. As the degree of oxidation increased, the orientation of the aromatic lattice fringes became more disordered, and the distortion degree increased. The distribution range of Y and T type dislocation structures, which were widely distributed in short (<0.59 nm) lattice fringes, increased, while that of spiral type dislocation structures, which were distributed in medium (0.59−0.99 nm) and long (1.00−2.49 nm) lattice fringes, decreased. In addition, the collapse and condensation of aromatic slices caused by continuous oxidation further weakened the $\pi-\pi$ stacking effect between aromatic rings, resulting in a decrease in the interlayer distance and stacking height. The advantages of HRTEM analysis were confirmed by XRD, SEM and FTIR analysis. This provides a new perspective on the oxidation phenomenon and enriches the examination of the low-temperature oxidation mechanism of coal.

1. INTRODUCTION

Coal is expected to remain the primary source of energy in China, accounting for approximately 60% of primary energy consumption by 2030.[1−4] To promote the efficient and clean use of coal, research in the field has emphasized the importance of studying the mechanisms of oxidative processes in coal.[5−7] Before, during, and after mining, oxidation occurs in all coals, leading to significant changes in their physical and chemical properties.[8,9] These changes include a decrease in the natural hydrophobicity of the coal grain surface, an increase in hydrophilicity, and a significant reduction in flammability. The processing properties of the coal are also affected, with a decline in the calorific value, thermal efficiency, and adhesiveness.[10−13] Such changes can result in the waste of coal resources and serious economic losses. Moreover, in certain conditions, the accumulation of heat can lead to spontaneous combustion, causing harm to the environment and human health.[14,15] Fires in sealed coal storage spaces or underground mining mines, as well as chain-triggered gas explosions, can have catastrophic

consequences.[16−18] Therefore, understanding the mechanism of low-temperature oxidation on coal is desirable.

Although the low-temperature oxidation of coal has been extensively studied,[19,20] the mechanism of this multi-stage oxidation reaction is complex.[21−23] Currently, modern physical analysis techniques, such as Fourier transform infrared spectroscopy (FTIR), X-ray photoelectron spectroscopy (XPS), and X-ray diffraction (XRD), are used to quantify the changes in functional groups in coal during different oxidation stages.[24−26] In the process of low-temperature oxidation of coal, the functional groups containing oxygen atoms (such as phenolic hydroxyl, carboxyl, ketone, and ether bonds) undergo significant changes. By measuring the content of the functional groups

containing oxygen in coal, the changes that occur in coal during the oxidation process can be quantified.[27−29] Coal is a chemically complex high molecular weight compound composed of multiple chemical bonds and functional groups. Therefore, it has multiple components and a hierarchical structure.[30−33] Observing the structural characteristics of coal can be achieved using high-resolution transmission electron microscopy (HRTEM) and scanning electron microscopy (SEM).[34−37] Among them, HRTEM is a high-resolution electron microscope based on transmission and diffraction electron beams, which can obtain the line image of aromatic lattice fringes in coal and directly reflect the atomic-level lattice information in coal structure.[38,39]

The use of HRTEM to observe and describe the morphology of aromatic lattice fringes has been extensively applied in coal. For example, Li et al.[40] used HRTEM to observe and analyze the structural evolution of aromatic lattice fringes during coal-to-graphite conversion; Yang et al.[41] investigate the structural changes of aromatic lattice fringes during the low-temperature pyrolysis of Xinjiang anthracite; while Chen et al.[42] characterized the genesis of aromatic clusters and graphite-like structures in thermally modified coal. However, studies on the influence of oxidative degree on the morphology, structure, and lattice parameters of non-caking coal from a mesoscopic perspective are still limited. the extraction, calculation, and statistical analysis of aromatic lattice fringes in HRTEM images are prerequisites for quantitative analysis of coal structure parameters.[43−45] Manual extraction (using ArcGIS software) and automatic extraction (using MATLAB software) are two main tools for extracting aromatic lattice fringes in coal.[46,47] Manual extraction is time-consuming and involves significant human intervention, while automatic extraction using software programs is simple and quick, but the accuracy cannot be guaranteed. This research integrated the above two methods to further improve the accuracy of identifying and extracting aromatic lattice fringes.

In this study, the aromatic lattice fringes of coal with different oxidation levels were analyzed using HRTEM images, and two extraction methods were adopted to characterize their arrangement and spatial scale distribution. The process quantification by which the coal aromatic structure changes with oxidation level. The length, angle, tortuosity, morphological distribution, layer spacing, and stacking height of the coal aromatic lattice fringes were investigated and compared with the crystal structure information obtained from XRD. Meanwhile, SEM was utilized to analyze the coal's microstructure, and FTIR tests were used to analyze the changes in surface functional group content of coals with different levels of oxidation. This study provides a deeper insight into the structure-property-behavior relationships of coals with different degrees of oxidation, and offers support and reference for further research on the microscopic mechanisms and performance of low-temperature coal oxidation.

2. MATERIALS AND METHODS

2.1. Sample. The sample was taken from the 10# coal seam in the Hebaopian mining area of the Hedong coalfield (Shanxi, China), with the regional stratigraphic column and sampling stratum shown in Figure 1. According to the National Standard of the People's Republic of China (Classification of Coal) GB/T 5751-2009, the coal sample belongs to the non-stick coal (code BN) in the bituminous coal series. After crushing and sieving,
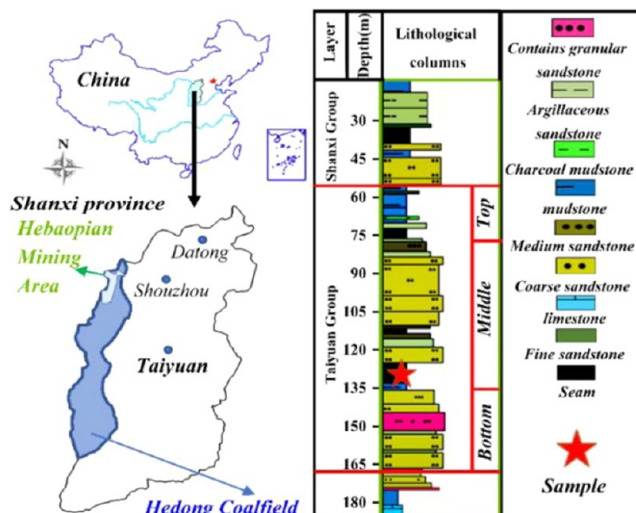

Figure 1. Location of the Hebaopian mining area, regional stratigraphic column, and sampling level.

the samples were selected to have a particle size of 200 mesh (0.074 mm).

The purpose of the study was to investigate the morphology and structural evolution of the aromatic fringes of coal with different degrees of low temperature oxidation. Therefore, 15 and 30 wt % H_2O_2 solutions were used to oxidize the coal particles.[48,49] By mixing 20 g of acid-washed coal particles with 100 mL of an aqueous H_2O_2 solution in a conical flask at room temperature for 24 h, the solution is vacuum filtered, then dried at 105 °C for 6 h and sealed for storage. The unoxidized coal is named PC; the oxidized coal treated with a 15% H_2O_2 solution is named OC15; and the oxidized coal treated with a 30% H_2O_2 solution is named OC30. The results of the elemental analysis of the raw and oxidized coal are shown in Table 1.

Table 1. Elemental Analysis of Three Coal Samples

sample	elemental analysis (wt %, d.m.m.f.)				
	C	H	O	N	S
PC	75.46	3.62	14.99	1.38	0.79
OC15	73.15	3.68	17.26	1.31	0.60
OC30	70.26	3.63	20.47	1.25	0.68

2.2. Experimental Tests and Methods. *2.2.1. HRTEM.* This examination employed a FEI Talos F200S transmission electron microscope (TEM) to conduct high-resolution transmission electron microscopy (HRTEM) experiments, operating at an acceleration voltage of 200 kV, with a point resolution of 0.19 nm and a lattice resolution of 0.14 nm. Three coal samples with different degrees of oxidation (PC, OC15, and OC30) were prepared, and 0.05 g of each sample was sonicated in ethanol for 30 min before being sprayed onto a copper mesh microgrid. The edge portion of the HRTEM image was selected for analysis to reduce the influence of thickness on aggregated lattice fringes and enhance the accuracy of the analysis.

2.2.2. HRTEM Lattice Fringe Extraction Methods. The ArcGIS software performs a vectorization operation on the HRTEM image, extracting the aromatic lattice fringes through manually drawn lines. The extraction principle is to find the start and end points of the raster fringes and draw a fold line along the geometric center. Color differentiation was based on the
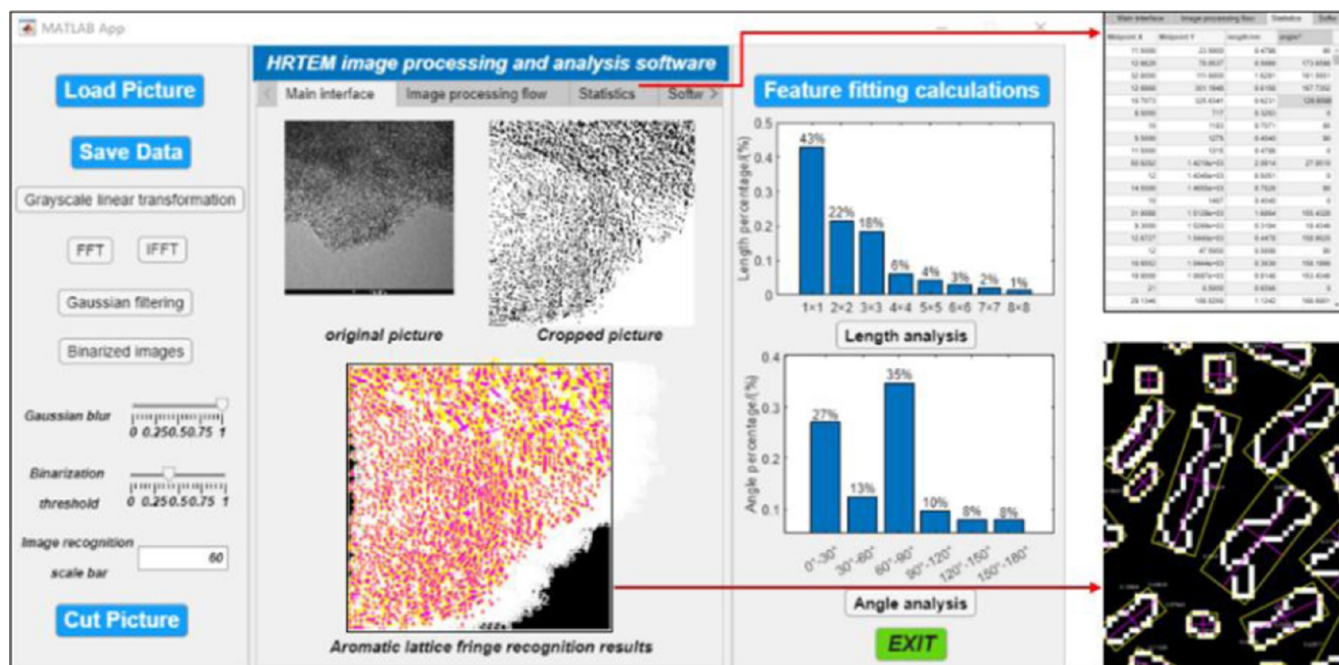
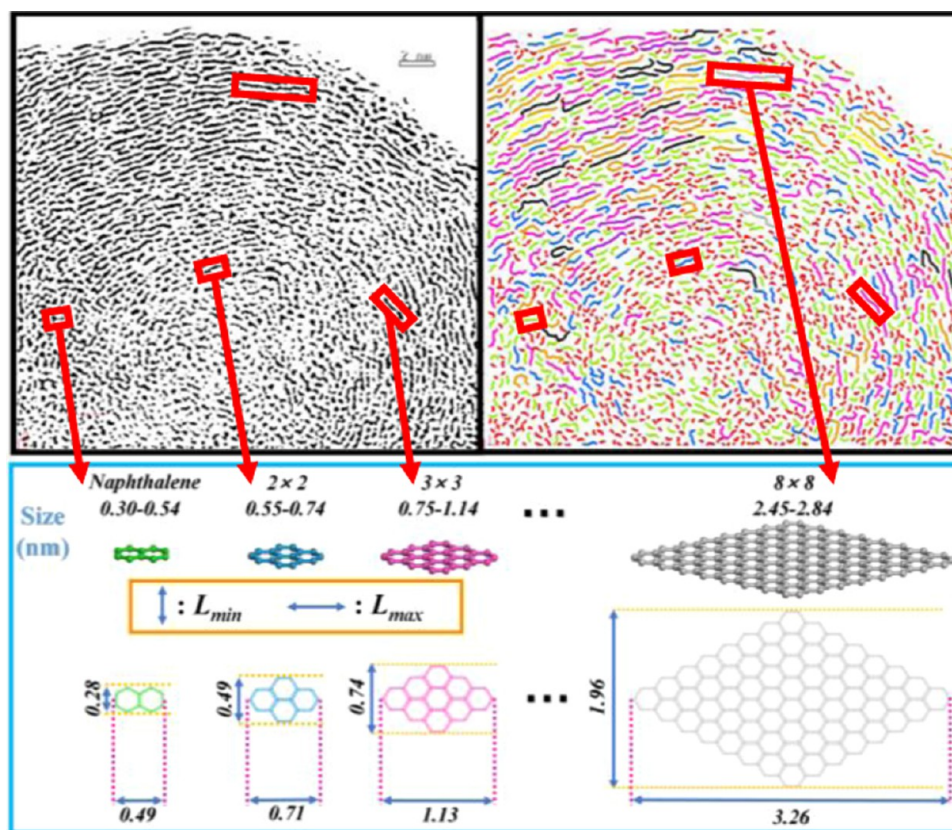**Figure 2.** MATLAB App program interface runtime diagram.

Figure 3. Correspondence of relations (HRTEM images-aromatic fringes-aromatic lamellae structure).

classification method proposed by Mathews et al.[50,51] The length, angle, and tortuosity of the aromatic fringes were quantitatively assessed with a Python script embedded in ArcGIS. Pre-processing of HRTEM images requires the use of Photoshop and digital micrographic software.

A MATLAB application designer based on digital morphology and image recognition algorithms has been written by the authors to automate the processing of HRTEM images of coal. Based on the basic MATLAB image processing techniques (contrast enhancement, grayscale transformation, denoising filtering, Gaussian blurring, forward and inverse Fourier
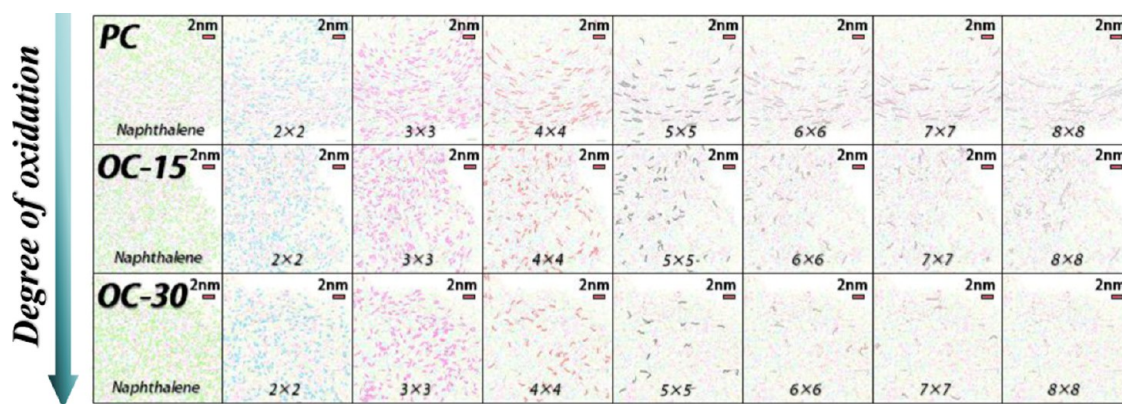
Figure 4. Aromatic fringes length distribution.

Table 2. Percentage of Aromatic Fringes Length (ArcGIS vs MATLAB)

sample	PC		OC15		OC30	
size (%)	ArcGIS	MATLAB	ArcGIS	MATLAB	ArcGIS	MATLAB
naphthalene	41.6	42.1	51.5	50.9	56.7	55.7
2 × 2	20.6	20.5	19.7	19.9	19.7	17.6
3 × 3	21.7	21.4	16.7	17.3	15.9	16.4
4 × 4	7.2	7.7	5.6	5.9	4.1	4.6
5 × 5	3.7	3.6	2.9	2.5	1.9	2.6
6 × 6	2.2	2.1	1.5	1.5	0.7	1.4
7 × 7	1.6	1.4	1.2	1.1	0.6	0.9
8 × 8	1.5	1.2	0.8	0.8	0.3	0.8

changes, binarization, and skeleton extraction), a multi-stage edge detection algorithm proposed by John Canny is introduced to further eliminate noise from adjacent isolated points, smooth the image contours, and improve the precision of aromatic streak recognition.[52] The detection of aromatic fringes is achieved by a computer vision recognition system. When the distance to the object is unknown, the concept of scale is implemented to achieve the calculation of a given unit of measurement and pixel scale, as well as the computer vision localization of aromatic fringes. By calculating the minimum outer rectangle of the aromatic fringes, structural parameters such as the length and angle of the aromatic lamellar skeleton in the coal can be obtained. The MATLAB program is shown in Figure 2.

2.2.3. XRD. The X-ray diffraction (XRD) were performed with a Panalytical Empyrean X-ray diffractometer. Cu Kα is used as the X-ray source with $\lambda = 1.54056$ Å. Coal samples with 0.1 g of uniform particles of 200 mesh or more were scanned from 5 to 90° at a speed of 2°/min over a scanning range of 2θ. The XRD spectra are resolved for overlapping peaks in Origin software, and microcrystalline structure parameters are obtained. The XRD tests are compared with the image processing results of HRTEM for validation.

2.2.4. SEM. Scanning electron microscopy (SEM) tests were performed using TESCAN MIRA LMS SEM, and 10 mg of each dried coal powder was directly glued to a conductive glue stick for testing. The micromorphological characteristics of the oxidized coal particles were examined.

2.2.5. FTIR. The surface functional group content of the coal samples was determined using a Thermo Scientific Nicolet iS20 Fourier transform infrared spectrophotometer from Thermo Fisher Scientific. Powder samples weighing 15 mg each were analyzed within the wavelength range of 4000−400 cm^{-1}. Before the analysis, the water content of the samples was removed using

the KBr method to minimize interference. OMNIC software was utilized for spectral calibration and data processing aimed at increasing the accuracy and reliability of the data obtained.

2.3. Aromatic Fringe Analysis Parameters. Hexagonal and parallelogram structures are often considered reasonable assumptions to represent the structure of coal aromatic units, while the projection length is considered to be an approximation as to the diameter of the aromatic sheet.[38,53] According to the parallelogram structure hypothesis for polycyclic aromatic hydrocarbons proposed by Van Niekerk and Mathews,[54] aromatic fringes are classified and attributed based on length elements, as shown in Figure 3. The aromatic laminar distribution is quantified according to the Louw method,[55] which assesses the effect of coal oxidation on the aromatic laminar structure by assessing the length of the aromatic fringes, thus extending the assessment information from 2D (aromatic fringes) to 3D (aromatic laminar).

3. RESULTS AND DISCUSSION

3.1. Fringe Length Distributions. Figure 4 shows the pseudo-color fringes in the HRTEM micrographs, with three distinct areas selected for image processing of each coal sample. From Figure 4, it is clear that the larger the size of the aromatic fringes, the smaller their number and distribution range; the number of medium (0.59−0.99 nm) and long (1.00−2.49 nm) fringes in the coal reduces significantly with the increase in oxidation. Three measurements of each coal sample are averaged by standard deviation, and the proportion of aromatic lattice streak lengths for the coals is shown in Table 2. In the three coals with different levels of oxidation, the lattice fringes consist mainly of aromatic rings close to the size of naphthalene (0.30−0.54 nm), with 41.6% for PC, 51.5% for OC15, and 56.7% for OC30. The number of naphthalene aromatic rings rises with the
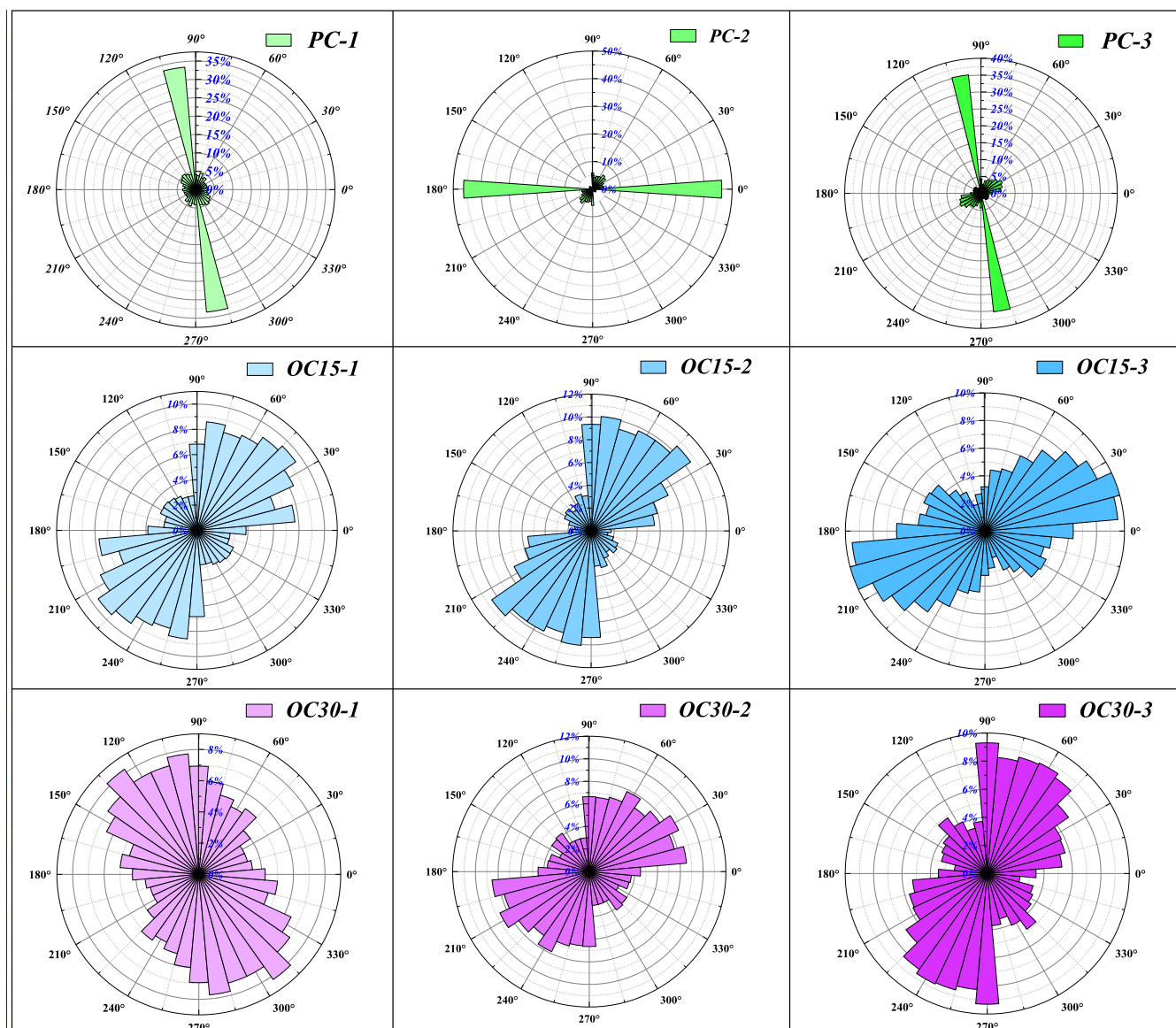
Figure 5. Rose diagram of the distribution of aromatic fringes.

degree of oxidation. Furthermore, the proportion of 2 × 2 aromatic rings (0.55−0.74 nm) in PC is 20.6%, which is slightly lower than the proportion of 3 × 3 aromatic rings (0.75−1.14 nm) (21.7%), in contrast to the situation in OC15 and OC30.

Meanwhile, the total number of 4 × 4, 5 × 5, 6 × 6, 7 × 7 and 8 × 8 aromatic rings accounted for 16.1% of the PC and only 12.1 and 7.7% of the OC15 and OC30, respectively. These values indicate that the changes in the length of the aromatic lattice fringes at lower temperatures are mainly related to the oxidation of H_2O_2, where the larger sized aromatic rings are broken down by H_2O_2 into smaller sized aromatic ring structures, oxidizing the R−OH and R−O−R bonds in the coals to produce groups such as −COOH and R-OH, and the weak non-covalent bonds in the coals are broken, generating more macromolecular fragments. The further percentage increase in the number of smaller-sized aromatic rings shows that the continuing break-down and oxidation of the large aromatic ring structures in the coal will be exacerbated by the deepening oxidation.

3.2. Fringe Orientation. The distribution of the angular orientation of the fringes is an important index of the structural stability of coal macromolecules.[56] The linear angular values of the fringes are extracted to quantify the orientation of the aromatic lamellae and to observe the impact of the degree of oxidation on them. It can be seen from the rose diagram in Figure 5 that the angular orientation of the fringes in the PC that is not oxidized with H_2O_2 is much more regular, the aromatic fringes are preferentially distributed between 0, 180, and 90−120°, and there is an obvious orderly orientation arrangement of the aromatic ring structure.

As a low to moderately altered bituminous coal that was considerably oxidized in the early stages of coal formation, the aromatic ring systems are shorter in size and form a less intense interaction of ordered aromatic systems than higher-order coals such as anthracite, therefore showing a more regular and orderly arrangement near the edges of the HRTEM images, where the aromatic fringes start to appear disordered in the interior of the HRTEM images. In OC15, the orientation of the aromatic fringes is mostly in the range of 0−90°; however, in OC30, the distribution of the aromatic fringes has a broader spread
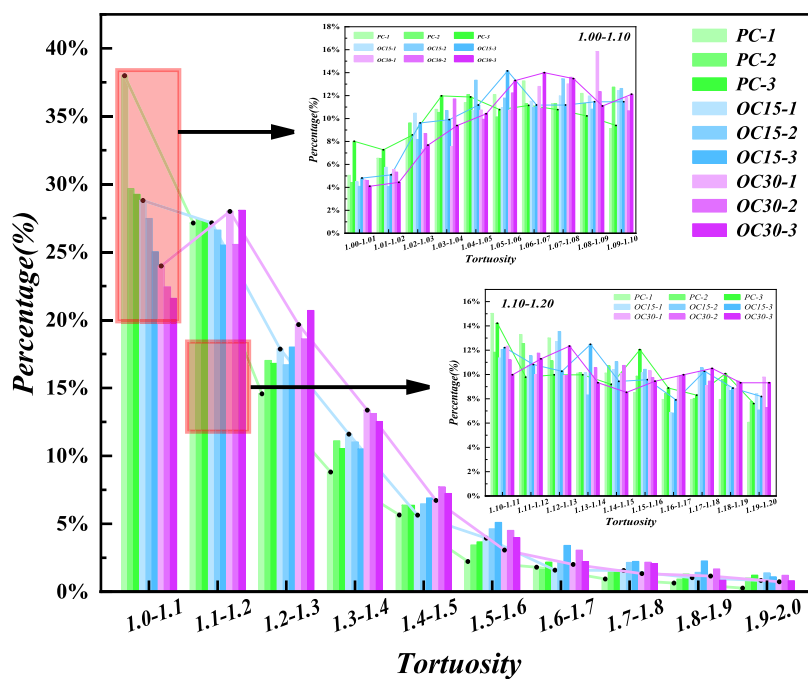
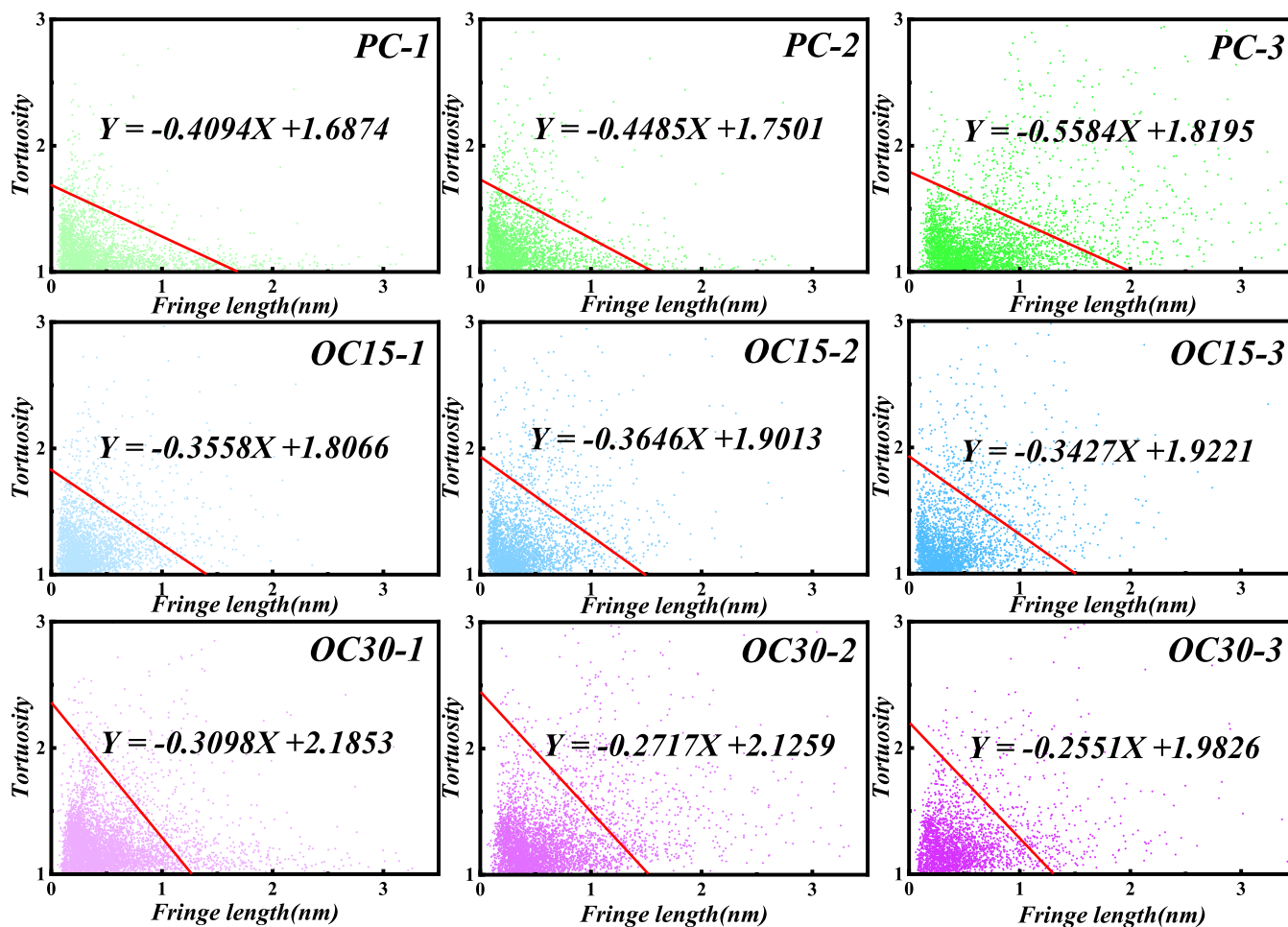**Figure 6.** Percentage tortuosity of nine groups of coal samples.

Figure 7. Length and tortuosity correlation for nine groups of coal samples.

compared with OC15, covering essentially 0−180° and showing a disorderly nature.

This situation reflects the constant movement of aromatic fragments released from the destruction of larger aromatic rings
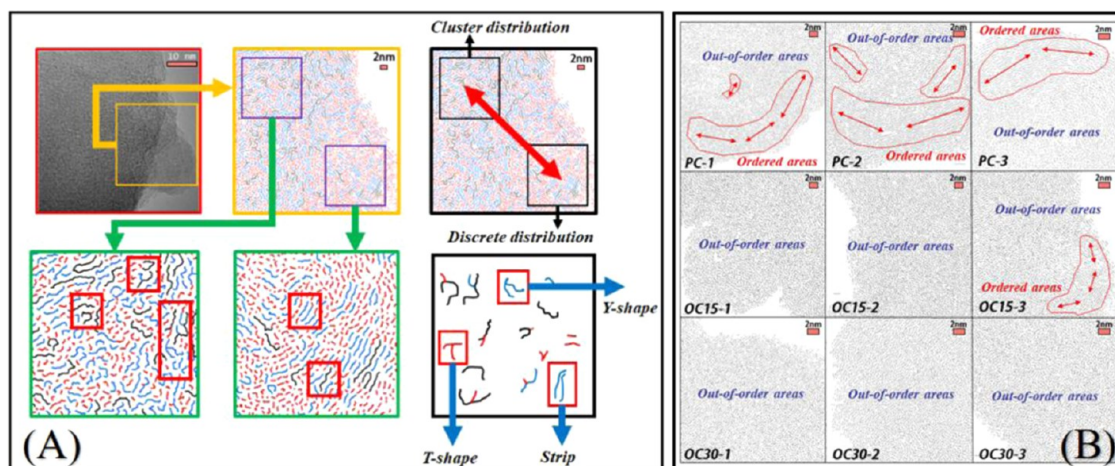
Figure 8. (A) Types of aromatic fringes accumulation and distribution in HRTEM; (B) Morphological distribution of nine groups of coal samples.
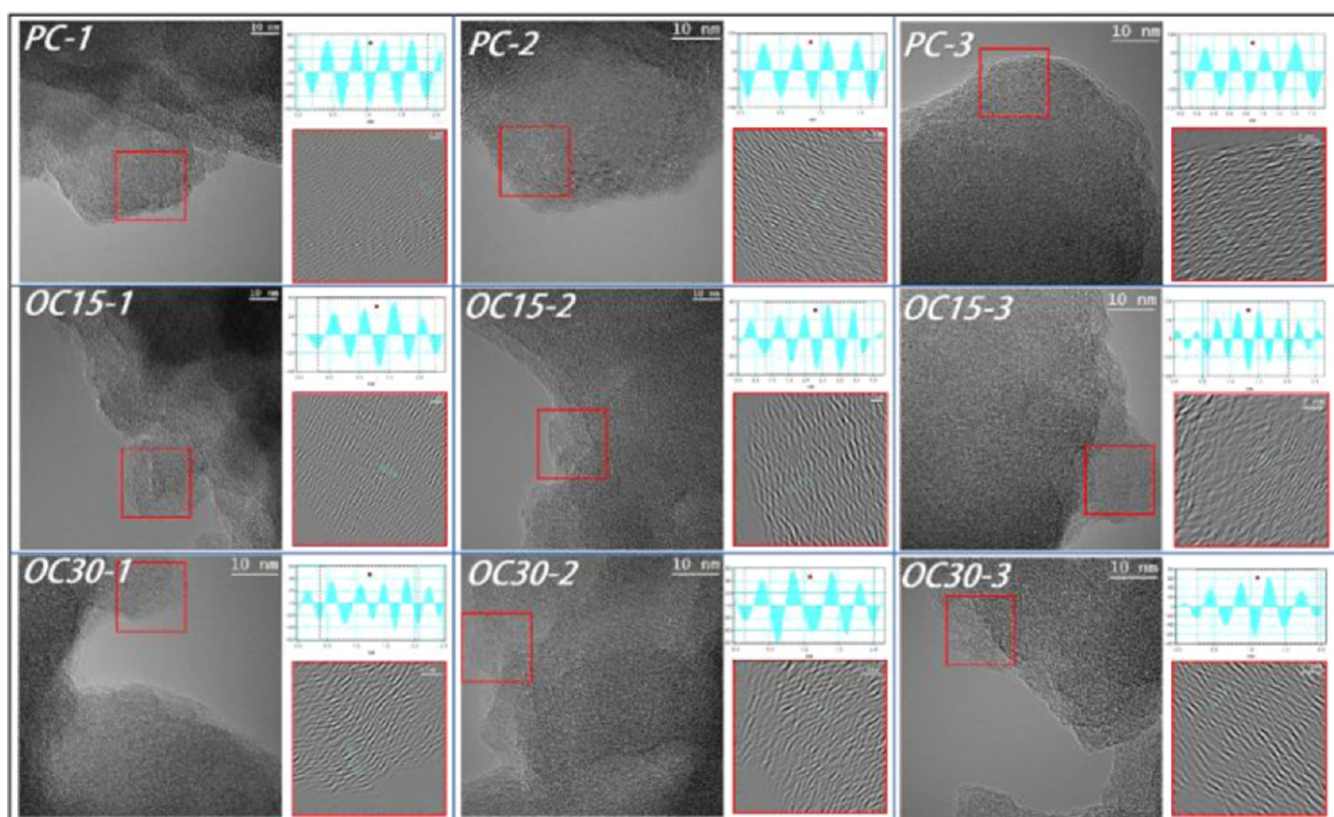

Figure 9. Measurement of aromatic fringe layer spacing and stacking height for coal samples.

during the oxidation of coal at low temperatures and the reversible reaction of non-covalent bonds leading to the continuous rotation and deformation of smaller aromatic rings to form lower-free-energy stacked pose conformations. Gradually, the preferred orientation of the aromatic structure becomes more disordered and disorganized with increasing oxidation.

3.3. Fringe Tortuousness. The tortuosity of the aromatic fringes is the ratio of the fringes' length to the linear distance between its two endpoints and reflects the horizontal fluctuation or tortuosity (non-linearity) of the single aromatic layer, The average tortuosity represents the linearity of the overall aromatic layer segment in the HRTEM image of the coal.[57] As shown in Figure 6, the relative number of aromatic fringes decreases with the increase in tortuosity for all coal samples. The three groups

of coal samples in PC have the highest proportion of aromatic fringes with tortuosity between 1.00 and 1.10, while the six groups of coal samples in OC15 and OC30 have tortuosity mostly between 1.10 and 1.20. Calculating the average values for the same type of coal samples indicated that the percentage of tortuosity between 1.00 and 1.10 consisted of PC (32.29%), OC15 (27.09%), and OC30 (22.66%). The closer the average tortuosity is to 1, the better the overall linearity of the aromatic layer is. PC shows a better overall linearity of the aromatic layer, while the linear relationship between the concentrations of OC15 and OC30 decrease as oxidation increases. This means that the tortuosity of the aromatic layer increases as oxidation deepens, transforming into a more non-linear lamellar structure.
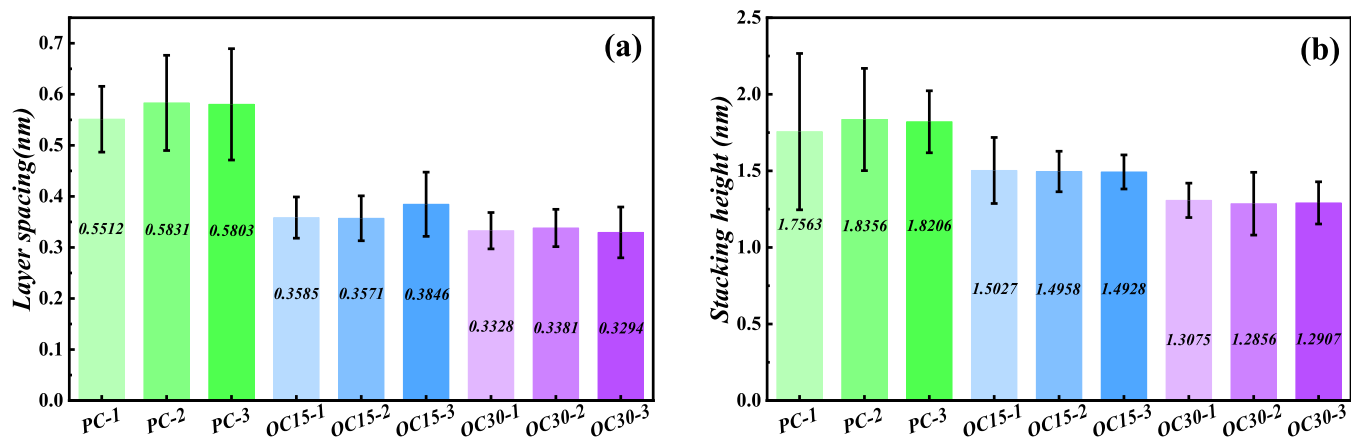
Figure 10. Comparison of aromatic fringe layer spacing (a) and stacking height (b).
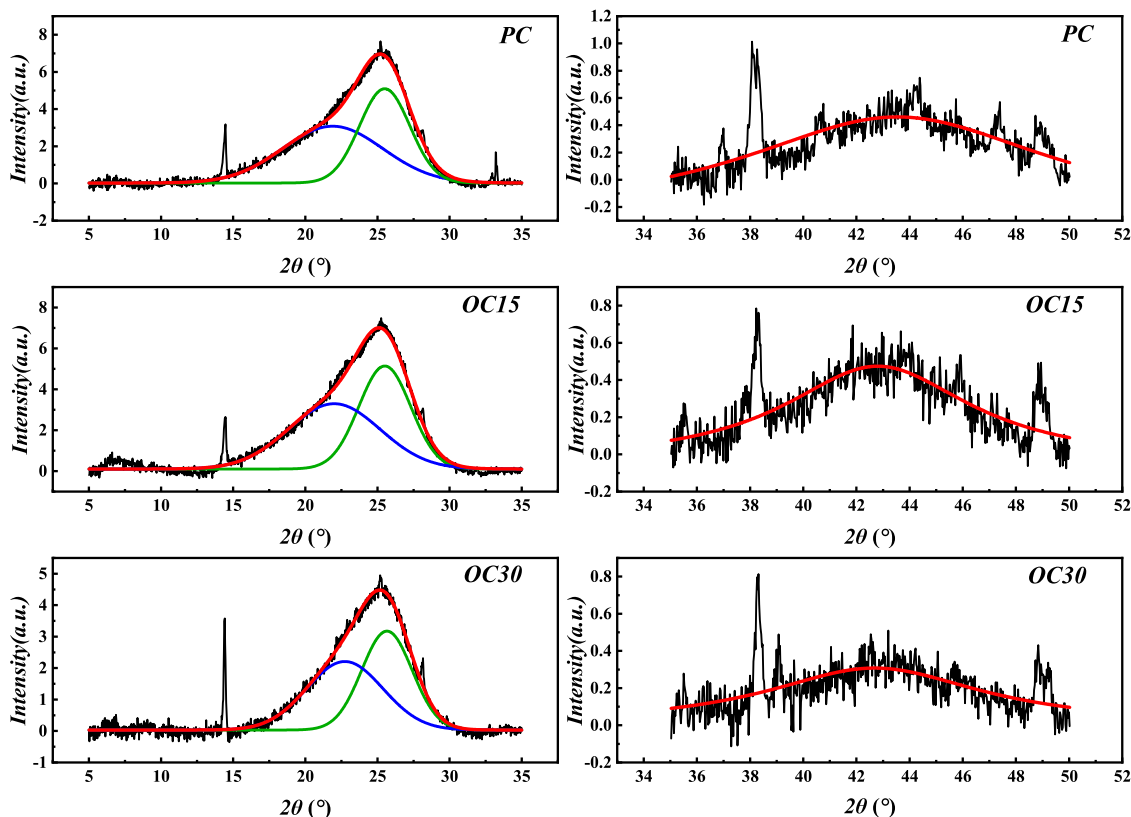

Figure 11. XRD-fitted profiles of PC, OC15, and OC30 coal samples.

This is attributed to the reduction in aromatic size, resulting in a weaker attraction between the aromatic lamellar systems.

Figure 7 shows the correlation between the length (X-axis) and tortuosity (Y-axis) of the aromatic fringes; most of the curved fringes in the nine groups of coal samples lie inside the range of the triangular box. The analysis of the data points within the triangular box shows that the tortuosity tends to decrease as the length increases, with some of the shorter fringes having greater tortuosity while most of the longer fringes having less tortuosity. It suggests that short fringes are the main component of curved fringes in the three different levels of oxidized coal. Calculating the average of the triangular box slope for the same type of coal samples, the following linear slope data are obtained: PC (−0.4721), OC15 (−0.3544), and OC30 (−0.2789). The slope decreases as the degree of oxidation increases, but the

tortuosity of the aromatic fringes of the same length increases instead. It indicates that although the medium and long fringes are continuously destroyed during the oxidation of the coal, a large number of short fringes still continue to be destroyed into smaller aromatic rings, and these short aromatic ring structures continue to be oxidized to produce various acidic groups.

3.4. Fringe Morphological Distribution. In the aromatic lattice fringes system of coal, most of the fringes are distributed in clusters or discrete states.[46] As an example, the HRTEM image (OC15-3) in Figure 8A shows the morphological distribution of aromatic lattice fringes in coal between unoxidized and deeply oxidized. The more common fringes morphologies are T-shaped dislocations, Y-shaped dislocations, and spiral fringes. Observation of Figure 8B reveals that spiral fringes dislocations are widely distributed in the PC coal samples
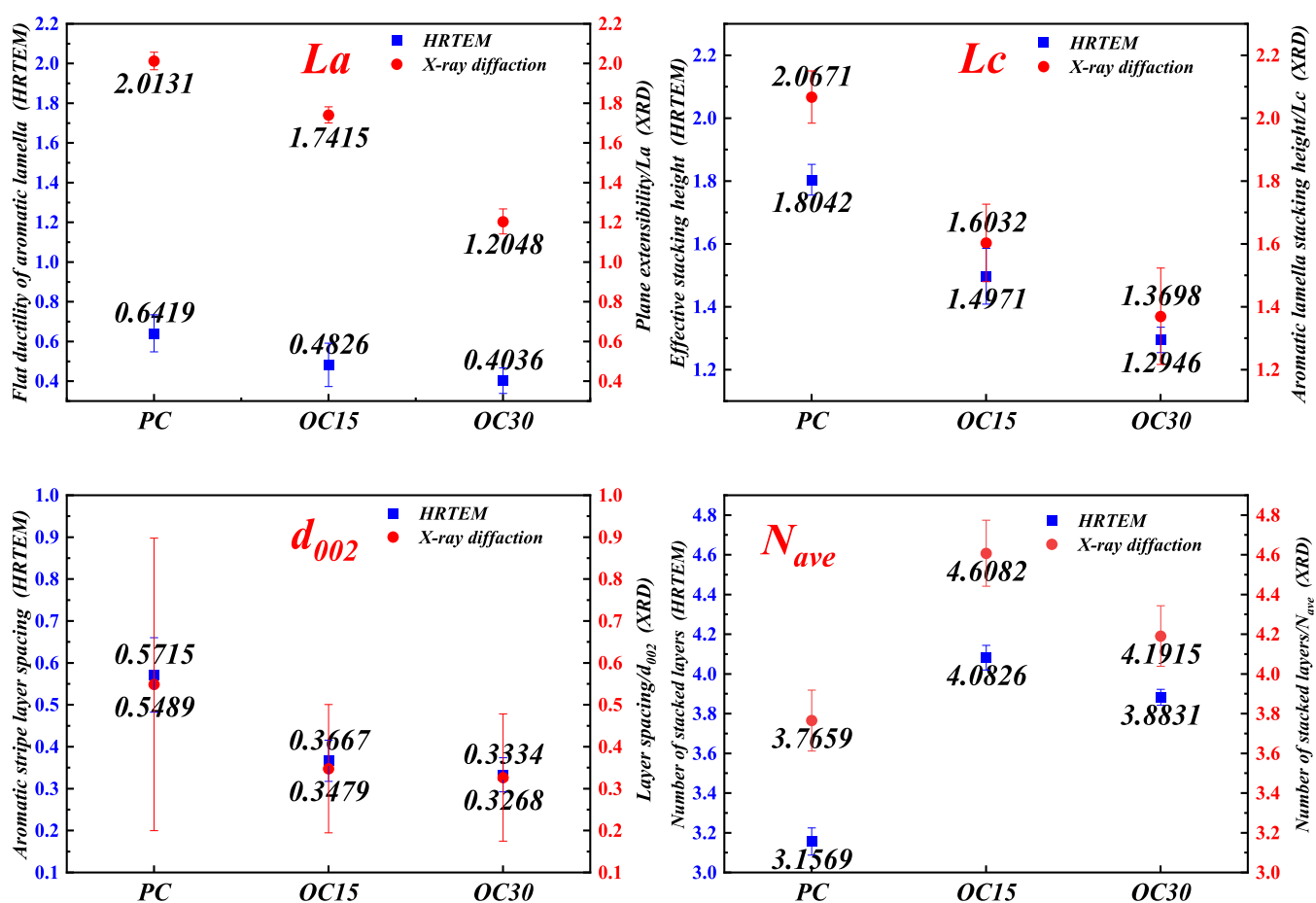
Figure 12. Comparison of XRD and HRTEM data (d_{002}, L_c, L_a, and N_{ave}).

and parts of the OC15 coal samples, rarely in the OC30 coal samples, mostly between medium (0.59−0.99 nm) and long (1.00−2.49 nm) fringes. In contrast, T and Y dislocation stacking geometries are distributed across all coal samples and more widely in oxidized coals OC15 and OC30, mainly in the short fringes (0.59 nm). It is also clear that the aggregate distribution of fringes becomes more obvious with increased oxidation.

3.5. Fringe Layer Spacing and Stacking Height. Parallel aromatic lamellae spacing and stacking heights are determined with digital micrographs and ArcGIS software. Figure 9 illustrates the measurements of the aromatic lamellae spacing in different areas of different coal samples. In Figure 10a, it can be seen that the aromatic lamellae spacing in the coal sample decreases as the degree of oxidation increases. Layer spacing values can be calculated by taking the average of samples from the same type of coal. PC (0.57 nm), OC15 (0.37 nm), and OC30 (0.33 nm). In Figure 10b, it is shown that the stacking height of the lattice fringes in the coal samples decreases with increasing oxidation. The greater the degree of oxidation, the more unevenly distributed the aromatic lattice fringes are found to be, showing very poor stacking characteristics. Similarly, lattice fringes stacking height values are obtained by calculating average values for coal samples of the same type. PC (1.8042 nm), OC15 (1.4971 nm), and OC30 (1.2946 nm).

Such a phenomenon demonstrates that during the oxidation of coal, the aromatic ring structure is continuously disrupted, and the aromatic fringes keep collapsing and condensing with each other. The longer aromatic layers contain more sp^2

hybridized carbon than the shorter ones, and their adjacent carbon and hydrogen atom orbitals overlap co-planarly to form σ-bonds.[58] Each hybridized p-orbital is parallel and overlaps to form dense polyaromatic planes. The larger dense polycyclic structure provides a larger off-domain space for electrons, thus providing the opportunity for increased $\pi-\pi$ stacking between aromatic systems.[59,60] However, $\pi-\pi$ stacking effects between aromatic systems are existent but weak because the non-stick coal itself is a low-order bituminous coal. During the process of successive oxidation of coals, the decomposition of medium-length fringes into short fringes and the virtual absence of $\pi-\pi$ interactions, which are predominantly present between the long fringes, lead to a gradual shift from a small number of coplanar-parallel (intercalated and parallel-displaced) stacking configurations to Y and T-shaped stacking geometries in the coals. This may be the principal reason for the reduction in layer spacing and stacking height in oxidized coals.

3.6. XRD vs HRTEM Results. Because of the non-homogeneous nature of coal, the aromatic part of the coal structure is capable of exhibiting crystalline anisotropy, and X-ray diffraction (XRD) is one of the methods employed to describe the structure of coal in its aggregated state.[61−63] The figure for 2θ on 5−35 and 35−50° is fitted to the split peaks as shown in Figure 11. The microcrystalline structures of three coals with different degrees of oxidation are analyzed: aromatic layer spacing (d_{002}), aromatic layer stacking height (L_c), aromatic layer ductility (L_a), and number of stacked layers (N_{ave}). According to the Bragg and Scherer equations,[64] the

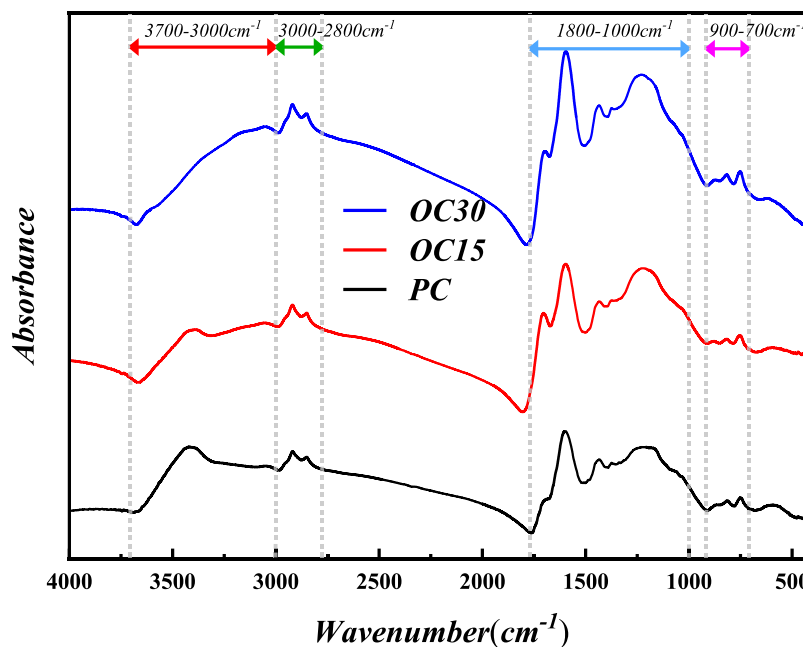**Figure 13.** SEM images of coal samples before and after oxidation.

Figure 14. FTIR spectra of PC, OC15, and OC30 coal samples.

characteristic structural parameters of the coals have been obtained as follows

$$d_{002} = \lambda / 2 \sin \theta_{002} \tag{1}$$

$$L_c = K_1 \lambda / \beta_{002} \cos \theta_{002} \tag{2}$$

$$L_a = K_2 \lambda / \beta_{10} \cos \theta_{10} \tag{3}$$

$$N_{ave} = L_c / d_{002} \tag{4}$$

where: d_{002} is the crystal plane spacing corresponding to peak 002 (nm); θ_{002} and θ_{10} are the Bragg angles (°) corresponding to the peak positions of peaks 002 and 10; λ is the X-ray wavelength (nm); β_{002} and β_{10} are the half-peak width values (rad) of bands 002 and 10; K_1 and K_2 are the microcrystal shape factors, K_1 = 0.94 and K_2 = 1.84. The d_{002} and L_c in HRTEM are the lattice fringes layer spacing and stacking height measured in 3.5, respectively, and L_a is the weighted average of the aromatic fringes' lengths.

The XRD and HRTEM processing results shown in Figure 12 indicate that most of the structural parameters are relatively compatible, and this is reflected in the layer spacing of the aromatic ring layers (d_{002}), the effective stacking height of the aromatic ring layers (L_c), and the number of stacking layers (N_{ave}). The significant difference in ductility (L_a) testing between the aromatic seams is mainly attributed to the large difference in testing principles between the two tests: XRD reflects average information about the coal structure, whereas

HRTEM testing reflects localized areas of the coal structure. The superiority of HRTEM compared to XRD is that the highly averaging effects of various structural parameters such as spacing d, crystallite size L_c, and crystallite diameter L_a are avoided.[65] Overall, the results of XRD and HRTEM are found to be relatively close, verifying the reliability and authenticity of the HRTEM processing results.

3.7. SEM Analysis. By using SEM to examine the morphological characteristics of the raw coal and coal samples treated with different levels of oxidation, a magnification of 2000x was used. As shown in the SEM image in Figure 13, the number of pores, cracks and tiny fragments on the surface of the raw coal was low. As the degree of oxidation deepened, a large number of pores and fragments were produced on the surface of OC15 and OC30, and the increased concentration of H_2O_2 caused more obvious damage to the surface morphology of the coal. the large number of pore structures produced on the surface of the oxidized coal provided a channel for further penetration of the oxidant. the SEM results strongly validated the data from the previous analysis, visually demonstrating the microstructural effects caused by oxidation on the coal surface.

3.8. FTIR Analysis. Figure 14 shows the infrared spectra of the PC, OC15, and OC30 coal samples. It can be seen from the figure that the three coal samples show similar absorption bands and characteristic absorption peaks, but the infrared spectral transmittance of the coal samples has changed because of the different degrees of oxidation. With increasing oxidation, the hydroxyl absorption of the coal samples near 3413 cm^{-1} is

decreasing, probably because the phenolic and alcohol hydroxyl groups are oxidized and broken into carboxylic acid groups or CO_2 and CO molecules, as supported by the enhancement of CO_2 and CO absorption near 2498 cm^{-1}. The IR transmittance of the C=C stretching vibration peak near 1594 cm^{-1} decreases slightly with oxidation, indicating that the aromatic ring is more stable and less susceptible to being oxidized. 2922 and 2848 cm^{-1} show decreasing transmittance of the methyl and methylene asymmetric stretching vibration peaks, reflecting the reduction of aliphatic and cycloalkanes after oxidation under H_2O_2. The content of C–O groups such as ether bonds near 1220 cm^{-1} is not dramatically changed, which is associated with the high stability of C–O groups like ether bonds. The carbonyl absorption near 1597 cm^{-1} is obviously increased, possibly under the action of H_2O_2 where C–O–C is broken down or carboxyl groups are formed directly. The FTIR results are similar to those from most researchers and support the feasibility and accuracy of the work in the previous section.

4. CONCLUSIONS

In the present study, we quantified the morphology and structural parameters of differently low-temperature oxidized non-caking coal at mesoscopic scale using HRTEM. We investigated the effect of oxidation on the aromatic lattice stripe arrangement of coal, which enriches the current knowledge of the structural evolution of coal under low-temperature oxidation. Based on our findings, we draw the following conclusion:

1. As the degree of coal oxidation increases, the amount of oxygen-containing functional groups increases. Simultaneously, the longer fringes of the coal break into smaller sizes through oxidation. The aromatic ring structure also disassembles and condenses, and the acidic groups accelerate the migration and twisting of the aromatic system. This results in the reduction of the π–π stacking interactions between the aromatic systems and causes the distribution of aromatic fringes to become more disordered and disorganized.

2. HRTEM images of the three types of coal samples show that short fringes (<0.59 nm) are always the main part of the aromatic composition structure of the non-stick coal before and after oxidation. Moreover, the percentage of aromatic ring structures with naphthalene (0.30–0.54 nm), 2 × 2 aromatic rings (0.55–0.74 nm), and 3 × 3 aromatic rings (0.74–1.14 nm) as the main units increased with increasing oxidation. The percentage reached 83.9% in PC, 87.9% in OC15, and 92.3% in OC30.

3. As the degree of oxidation deepens, the strip dislocation content of the aromatic structure reduces, and the T and Y-shaped dislocation content rises; most of the fringes gradually change from a discrete distribution state to a cluster distribution state, and the arrangement of the aromatic fringes turns from orderly to disorderly; Angular changes in the orientation distribution increase, and change from bipolar to multipolar; The tortuosity continuously diminishes as the strip length increases, and in the coals under different degrees of oxidation, the tortuosity of the aromatic fringes of the same length also varies, showing an alignment pattern of PC < OC15 < OC30.

4. There is little difference in the obtained information on the length, angle, and tortuosity of the aromatic lattice fringes between the two statistical methods of ArcGIS and MATLAB, which further clarifies the authenticity and accuracy of the experimental data. The MATLAB App program written by the authors greatly reduces the workload and improves efficiency.

5. Analyzing the microcrystalline structure parameters (d_{002}, L_c, L_a, and N_{ave}) of three coals with different degrees of oxidation via X-ray diffraction (XRD), the experimental results are mostly close to the HRTEM processed data, indicating the accuracy of the combination of the various methods used. However, in the comparison of the average diameter of the aromatic lamellae (L_a), the HRTEM test results are significantly different from XRD, illustrating that differences in testing principles can have an impact on the experimental results.

Combined with characterization tools such as SEM and FTIR, surface microstructure, property and reactive group changes before and after coal oxidation are obtained, which can better assist in illustrating the microscopic change mechanism of coal oxidation at low temperatures.

■ AUTHOR INFORMATION

Corresponding Authors

Guochao Yan — *School of Mining Engineering, Taiyuan University of Technology, Taiyuan 030024, China;* orcid.org/0009-0001-9491-6911; Email: yanguochao@tyut.edu.cn

Shaoqi Kong — *School of Mining Engineering, Taiyuan University of Technology, Taiyuan 030024, China;* Email: kongshaoqi@tyut.edu.cn

Authors

Jiajun Li — *School of Mining Engineering, Taiyuan University of Technology, Taiyuan 030024, China*

Zhen Li — *College of Mechanical and Vehicle Engineering, Taiyuan University of Technology, Taiyuan 030024, China*

Gang Li — *School of Mining Engineering, Taiyuan University of Technology, Taiyuan 030024, China*

Xuyang Bai — *School of Mining Engineering, Taiyuan University of Technology, Taiyuan 030024, China*

Jiawei Zhang — *School of Mining Engineering, Taiyuan University of Technology, Taiyuan 030024, China*

Complete contact information is available at:
https://pubs.acs.org/10.1021/acsomega.3c02766

Notes

The authors declare no competing financial interest.

■ ACKNOWLEDGMENTS

■ REFERENCES

(1) Zhang, B.; Luo, Z. F.; Zhao, Y. M.; Lv, B.; Song, S. L.; Duan, C. L.; Chen, Z. Q. Effect of a high-density coarse-particle layer on the stability

of a gas−solid fluidized bed for dry coal beneficiation. *Int. J. Miner. Process.* **2014**, *132*, 8−16.

(2) Wang, Q.; Li, R. Decline in China's coal consumption: An evidence of peak coal or a temporary blip? *Energy Policy* **2017**, *108*, 696−701.

(3) Andreoni, V. Drivers of coal consumption changes: A decomposition analysis for Chinese regions. *Energy* **2022**, *242*, No. 122975.

(4) Wang, Q.; Li, R. Journey to burning half of global coal: Trajectory and drivers of China's coal use. *Renewable Sustainable Energy Rev.* **2016**, *58*, 341−346.

(5) Li, D.; Wu, D.; Xu, F.; Lai, J.; Shao, L. Literature overview of Chinese research in the field of better coal utilization. *J. Cleaner Prod.* **2018**, *185*, 959−980.

(6) Di Gianfrancesco, A. 19 - Worldwide overview and trend for clean and efficient use of coal. In *Materials for Ultra-Supercritical and Advanced Ultra-Supercritical Power Plants*; Di Gianfrancesco, A., Ed.; Woodhead Publishing, 2017; pp 643−687.

(7) Zhang, B.; Wang, S.; Wang, D.; Wang, Q.; Yang, X.; Tong, R. Air quality changes in China 2013−2020: Effectiveness of clean coal technology policies. *J. Cleaner Prod.* **2022**, *366*, No. 132961.

(8) Zhou, D.; Lu, W.; Li, J.; Song, Y.; Wu, C. Reactive adsorption mechanism of O2 onto coal vitrinite during the low temperature oxidation process. *Fuel* **2022**, *308*, No. 121802.

(9) Yutao, Z.; Yuanbo, Z.; Yaqing, L.; Xueqiang, S.; Yujie, Z. Heat effects and kinetics of coal spontaneous combustion at various oxygen contents. *Energy* **2021**, *234*, No. 121299.

(10) Chen, S.; Tang, L.; Tao, X.; Chen, L.; Yang, Z.; Li, L. Effect of oxidation processing on the surface properties and floatability of Meizhiyou long-flame coal. *Fuel* **2017**, *210*, 177−186.

(11) Sarikaya, M.; Özbayoğlu, G. Flotation characteristics of oxidized coal. *Fuel* **1995**, *74*, 291−294.

(12) Chang, Z.; Chen, X.; Peng, Y. Understanding and improving the flotation of coals with different degrees of surface oxidation. *Powder Technol.* **2017**, *321*, 190−196.

(13) Xia, W.; Yang, J.; Liang, C. A short review of improvement in flotation of low rank/oxidized coals by pretreatments. *Powder Technol.* **2013**, *237*, 1−8.

(14) Deng, J.; Zhao, J.; Zhang, Y.; Huang, A.; Liu, X.; Zhai, X.; Wang, C. Thermal analysis of spontaneous combustion behavior of partially oxidized coal. *Process Saf. Environ. Prot.* **2016**, *104*, 218−224.

(15) Lü, H.-F.; Deng, J.; Li, D.-J.; Xu, F.; Xiao, Y.; Shu, C.-M. Effect of oxidation temperature and oxygen concentration on macro characteristics of pre-oxidised coal spontaneous combustion process. *Energy* **2021**, *227*, No. 120431.

(16) Xiao, Y.; Ren, S.-J.; Deng, J.; Shu, C.-M. Comparative analysis of thermokinetic behavior and gaseous products between first and second coal spontaneous combustion. *Fuel* **2018**, *227*, 325−333.

(17) Szurgacz, D.; Tutak, M.; Brodny, J.; Sobik, L.; Zhironkina, O. The method of combating coal spontaneous combustion hazard in goafs—a case study. *Energies* **2020**, *13*, No. 4538.

(18) Liang, Y.; Zhang, J.; Wang, L.; Luo, H.; Ren, T. Forecasting spontaneous combustion of coal in underground coal mines by index gases: A review. *J. Loss Prev. Process Ind.* **2019**, *57*, 208−222.

(19) Xi, Z.; Jin, B.; Shan, Z. Reaction mechanisms involving peroxy radical in the low-temperature oxidation of coal. *Fuel* **2021**, *300*, No. 120943.

(20) Liu, S.; Wu, Y.; Zhou, C.; Wu, J.; Zhang, Y. Study on the CO formation mechanism during coal ambient temperature oxidation. *Energies* **2020**, *13*, No. 2587.

(21) Zhang, Y.; Wu, J.; Chang, L.; Wang, J.; Xue, S.; Li, Z. Kinetic and thermodynamic studies on the mechanism of low-temperature oxidation of coal: A case study of Shendong coal (China). *Int. J. Coal Geol.* **2013**, *120*, 41−49.

(22) Xiao, Y.; Guo, T.; Shu, C.-M.; Li, Q.-W.; Li, D.-J.; Chen, L.-G. Effects of oxygen concentrations on the coal oxidation characteristics and functional groups. *J. Therm. Anal. Calorim.* **2020**, *142*, 899−912.

(23) Liotta, R.; Brons, G.; Isaacs, J. Oxidative weathering of Illinois No. 6 coal. *Fuel* **1983**, *62*, 781−791.

(24) Liang, Y.; Tian, F.; Luo, H.; Tang, H. Characteristics of coal re-oxidation based on microstructural and spectral observation. *Int. J. Min. Sci. Technol.* **2015**, *25*, 749−754.

(25) Xia, W.; Yang, J.; Liang, C. Investigation of changes in surface properties of bituminous coal during natural weathering processes by XPS and SEM. *Appl. Surf. Sci.* **2014**, *293*, 293−298.

(26) Zhou, C.; Zhang, Y.; Wang, J.; Xue, S.; Wu, J.; Chang, L. Study on the relationship between microscopic functional group and coal mass changes during low-temperature oxidation of coal. *Int. J. Coal Geol.* **2017**, *171*, 212−222.

(27) Wang, K.; Deng, J.; Zhang, Y.-n.; Wang, C.-p. Kinetics and mechanisms of coal oxidation mass gain phenomenon by TG−FTIR and in situ IR analysis. *J. Therm. Anal. Calorim.* **2018**, *132*, 591−598.

(28) Zhang, Y.; Wang, J.; Xue, S.; Wu, J.; Chang, L.; Li, Z. Kinetic study on changes in methyl and methylene groups during low-temperature oxidation of coal via in-situ FTIR. *Int. J. Coal Geol.* **2016**, *154-155*, 155−164.

(29) Zhang, W.; Jiang, S.; Wang, K.; Wang, L.; Xu, Y.; Wu, Z.; Shao, H.; Wang, Y.; Miao, M. Thermogravimetric Dynamics and FTIR analysis on oxidation properties of low-rank coal at low and moderate temperatures. *Int. J. Coal Prep. Util.* **2015**, *35*, 39−50.

(30) Marzec, A. Towards an understanding of the coal structure: a review. *Fuel Process. Technol.* **2002**, *77-78*, 25−32.

(31) Qin, Z. New advances in coal structure model. *Int. J. Min. Sci. Technol.* **2018**, *28*, 541−559.

(32) Haenel, M. W. Recent progress in coal structure research. *Fuel* **1992**, *71*, 1211−1223.

(33) Marzec, A. Macromolecular and molecular model of coal structure. *Fuel Process. Technol.* **1986**, *14*, 39−46.

(34) Rouzaud, J.-N.; Clinard, C. Quantitative high-resolution transmission electron microscopy: a promising tool for carbon materials characterization. *Fuel Process. Technol.* **2002**, *77-78*, 229−235.

(35) Kondo, Y.; Ohi, K.; Ishibashi, Y.; Hirano, H.; Harada, Y.; Takayanagi, K.; Tanishiro, Y.; Kobayashi, K.; Yagi, K. Design and development of an ultrahigh vacuum high-resolution transmission electron microscope. *Ultramicroscopy* **1991**, *35*, 111−118.

(36) Palotás, Á. B.; Rainey, L. C.; Feldermann, C. J.; Sarofim, A. F.; Vander Sande, J. B. Soot morphology: An application of image analysis in high-resolution transmission electron microscopy. *Microsc. Res. Tech.* **1996**, *33*, 266−278.

(37) Zhou, W.; Apkarian, R.; Wang, Z. L.; Joy, D. Fundamentals of Scanning Electron Microscopy (SEM). In *Scanning Microscopy for Nanotechnology: Techniques and Applications*; Zhou, W.; Wang, Z. L., Eds.; Springer: New York, 2007; pp 1−40.

(38) Sharma, A.; Kyotani, T.; Tomita, A. A new quantitative approach for microstructural analysis of coal char using HRTEM images. *Fuel* **1999**, *78*, 1203−1212.

(39) Mathews, J. P.; Cody, G. D.; Sharma, A. The structural alignment of coal as measured by image analysis of HRTEM fringes.

(40) Li, J.; Qin, Y.; Chen, Y.; Song, Y.; Wang, Z. HRTEM observation of morphological and structural evolution of aromatic fringes during the transition from coal to graphite. *Carbon* **2022**, *187*, 133−144.

(41) Yang, W.; Toth, P.; Song, Y.; Li, W. Structural alterations of aromatic fringes by HRTEM for Xinjing Vitrinite-rich anthracite: Impact of low-temperature pyrolysis. *Thermochim. Acta* **2022**, *713*, No. 179230.

(42) Chen, H.; Wang, S.; Tang, Y.; Zeng, F.; Schobert, H. H.; Zhang, X. Aromatic cluster and graphite-like structure distinguished by HRTEM in thermally altered coal and their genesis. *Fuel* **2021**, *292*, No. 120373.

(43) Yehliu, K.; Vander Wal, R. L.; Boehman, A. L. A comparison of soot nanostructure obtained using two high resolution transmission electron microscopy image analysis algorithms. *Carbon* **2011**, *49*, 4256−4268.

(44) Yehliu, K.; Vander Wal, R. L.; Boehman, A. L. Development of an HRTEM image analysis method to quantify carbon nanostructure. *Combust. Flame* **2011**, *158*, 1837−1851.

(45) Shim, H.-S.; Hurt, R. H.; Yang, N. Y. C. A methodology for analysis of 002 lattice fringe images and its application to combustion-derived carbons. *Carbon* **2000**, *38*, 29−45.

(46) Liu, L.; Du, M.; Li, G.; Schobert, H. H.; Fan, J.; Liu, J.; Wang, Q. Structure and evolution features of cutinite with different coal rank from stacking and arrangement of aromatic fringes in HRTEM. *Fuel* **2022**, *326*, No. 124998.

(47) Wang, S.; Chen, H.; Zhang, X. Transformation of aromatic structure of vitrinite with different coal ranks by HRTEM in situ heating. *Fuel* **2020**, *260*, No. 116309.

(48) Liu, Z.-X.; Liu, Z.-C.; Zong, Z.-M.; Wei, X.-Y.; Wang, J.; Lee, C. W. GC/MS Analysis of Water-Soluble Products from the Mild Oxidation of Longkou Brown Coal with H2O2. *Energy Fuels* **2003**, *17*, 424−426.

(49) Tian, Y.; Qin, Z.; Li, B. Preparation and H2O2 oxidation of extract. *Int. J. Min. Sci. Technol.* **2012**, *22*, 731−734.

(50) Zhong, Q.; Mao, Q.; Zhang, L.; Xiang, J.; Xiao, J.; Mathews, J. P. Structural features of Qingdao petroleum coke from HRTEM lattice fringes: Distributions of length, orientation, stacking, curvature, and a large-scale image-guided 3D atomistic representation. *Carbon* **2018**, *129*, 790−802.

(51) Mathews, J. P.; Sharma, A. The structural alignment of coal and the analogous case of Argonne Upper Freeport coal. *Fuel* **2012**, *95*, 19−24.

(52) Canny, J. A Computational Approach to Edge Detection. *IEEE Trans. Pattern Anal. Mach. Intell.* **1986**, *8*, 679−698.

(53) Huang, Y.; Cannon, F. S.; Watson, J. K.; Reznik, B.; Mathews, J. P. Activated carbon efficient atomistic model construction that depicts experimentally-determined characteristics. *Carbon* **2015**, *83*, 1−14.

(54) Niekerk, D. V.; Mathews, J. P. Molecular representations of Permian-aged vitrinite-rich and inertinite-rich South African coals. *Fuel* **2010**, *89*, 73−82.

(55) Wang, Ca.; Watson, J. K.; Louw, E.; Mathews, J. P. Construction Strategy for Atomistic Models of Coal Chars Capturing Stacking Diversity and Pore Size Distribution. *Energy Fuels* **2015**, *29*, 4814−4826.

(56) Yuan, L.; Liu, Q.; Mathews, J. P.; Zhang, H.; Wu, Y. Quantifying the Structural Transitions of Chinese Coal to Coal-Derived Natural Graphite by XRD, Raman Spectroscopy, and HRTEM Image Analyses. *Energy Fuels* **2021**, *35*, 2335−2346.

(57) Wang, X.; Wang, S.; Hao, C.; Zhao, Y.; Song, X. Quantifying orientation and curvature in HRTEM lattice fringe micrographs of naturally thermally altered coals: New insights from a structural evolution perspective. *Fuel* **2022**, *309*, No. 122180.

(58) Foster, H. H. Cylinder Art. *Design* **1969**, *71*, 4−6.

(59) Liu, S.; Zhang, Y.; Tuo, K.; Wang, L.; Chen, G. Structure, electrical conductivity, and dielectric properties of semi-coke derived from microwave-pyrolyzed low-rank coal. *Fuel Process. Technol.* **2018**, *178*, 139−147.

(60) Mallya, N.; Stock, L. M. The alkylation of high rank coals. Non-covalent bonding interactions. *Fuel* **1986**, *65*, 736−738.

(61) Van Niekerk, D.; Pugmire, R. J.; Solum, M. S.; Painter, P. C.; Mathews, J. P. Structural characterization of vitrinite-rich and inertinite-rich Permian-aged South African bituminous coals. *Int. J. Coal Geol.* **2008**, *76*, 290−300.

(62) Takagi, H.; Maruyama, K.; Yoshizawa, N.; Yamada, Y.; Sato, Y. XRD analysis of carbon stacking structure in coal during heat treatment. *Fuel* **2004**, *83*, 2427−2433.

(63) Jiang, J.; Yang, W.; Cheng, Y.; Liu, Z.; Zhang, Q.; Zhao, K. Molecular structure characterization of middle-high rank coal via XRD, Raman and FTIR spectroscopy: Implications for coalification. *Fuel* **2019**, *239*, 559−572.

(64) Feng, B.; Bhatia, S. K.; Barry, J. C. Structural ordering of coal char during heat treatment and its impact on reactivity. *Carbon* **2002**, *40*, 481−496.

(65) Sharma, A.; Kyotani, T.; Tomita, A. Comparison of structural parameters of PF carbon from XRD and HRTEM techniques. *Carbon* **2000**, *38*, 1977−1984.